

Correlated Feature Aggregation by Region Helps Distinguish Aggressive from Indolent Clear Cell Renal Cell Carcinoma Subtypes on CT

Karin Stacke^{a,b,c,*}, Indrani Bhattacharya^c, Justin R. Tse^c, James D. Brooks^d, Geoffrey A. Sonn^{c,d,1} and Mirabela Rusu^{c,**,1}

^aDivision for Media and Information Technology, Department of Science and Technology, Linköping University, Linköping, Sweden

^bSectra, Linköping, Sweden

^cDepartment of Radiology, Stanford University, Stanford, USA

^dDepartment of Urology, Stanford University, Stanford, USA

ARTICLE INFO

Keywords:

Renal Cell Carcinoma
Clear Cell Renal Cell Carcinoma
Prostate cancer
Machine learning
Deep learning
Correlated Feature Learning
Radiology-Pathology fusion
Multi-modal

ABSTRACT

Renal cell carcinoma (RCC) is a common cancer that varies in clinical behavior. Indolent RCC is often low-grade without necrosis and can be monitored without treatment. Aggressive RCC is often high-grade and can cause metastasis and death if not promptly detected and treated. Clear cell RCC is the most common subtype of RCC with a high degree of aggressive cases. While most kidney cancers are detected on CT scans, grading is based on histology from invasive biopsy or surgery. Determining aggressiveness on CT images would be an important clinical advance as it would facilitate risk stratification and treatment planning. The aim of this study is to use machine learning methods to identify radiology features that correlate with features on pathology to facilitate assessment of cancer aggressiveness on CT images instead of histology. This paper presents a novel automated method, Correlated Feature Aggregation By Region (CorrFABR), for classifying aggressiveness of clear cell RCC by leveraging correlations between radiology and corresponding unaligned pathology images. CorrFABR consists of three main steps: (1) *Feature Aggregation* where region-level features are extracted from radiology and pathology images, (2) *Fusion* where radiology features correlated with pathology features are learned on a region level, and (3) *Prediction* where the learned correlated features are used to distinguish aggressive from indolent clear cell RCC using CT alone as input. Thus, during training, CorrFABR learns from both radiology and pathology images, but during inference, CorrFABR will distinguish aggressive from indolent clear cell RCC using CT alone, in the absence of pathology images. CorrFABR improved classification performance over radiology features alone, with an increase in binary classification F1-score from 0.68 ± 0.04 to 0.73 ± 0.03 . This demonstrates the potential of incorporating pathology disease characteristics for improved classification of aggressiveness of clear cell RCC on CT images.

1. Introduction

In 2021, there were nearly 500 000 new renal cell carcinoma (RCC) cases diagnosed, and 200 000 reported deaths world-wide (Sung et al., 2021). Increased utilization of abdominal imaging has led to greatly increased detection of incidental renal masses (Capitanio and Montorsi, 2016; Capitanio et al., 2019). Radiological imaging, such as computed tomography (CT), plays a vital role in risk assessment and treatment planning for these renal masses, by distinguishing benign masses from renal cell carcinoma, and by characterizing the aggressiveness of malignant masses (de Leon and Pedrosa, 2017).

Clear cell RCC is the most common subtype ($\approx 75\%$), accountable for the majority of RCC deaths (Hsieh et al., 2017). Although clear cell RCC is asymptomatic in early stages, 25% to 30% of patients have tumors that have metastasized at the time of diagnosis (Rasmussen et al., 2022;

Padala et al., 2020). The prognosis of clear cell RCC depends on the aggressiveness of the mass, with higher tumor grade and the presence of necrosis being correlated with worse clinical outcomes (Minardi et al., 2005; Zhang et al., 2018; Moch et al., 2016).

The aggressiveness of clear cell RCC using tumor grade and necrosis is assessed on pathology images of tissue collected via biopsy or surgery. These invasive procedures are often associated with adverse side effects of bleeding, pain, and infection. Making this assessment on non-invasive radiology images, based on features like tumor grade and necrosis, can help decide the optimum management strategy, and prevent overtreatment and adverse side effects in patients with indolent disease (Rasmussen et al., 2022; Campbell et al., 2017; Rosales et al., 2010).

While there are clear clinical benefits of classifying aggressiveness of clear cell RCC on radiology images, the classification is challenging due to the subtle and overlapping features of the two classes (indolent and aggressive) (Morshid et al., 2021; Hötter et al., 2016). Correlating radiology and pathology features may help differentiate between the radiological appearance of aggressive and indolent clear cell RCC masses. Machine learning methods may help in

*Corresponding author

**Principal corresponding author

Email addresses: karin.stacke@liu.se (K. Stacke);

mirabela.rusu@stanford.edu (M. Rusu)

ORCID(s): 0000-0003-1066-3070 (K. Stacke)

¹Equally contributed as senior authors.

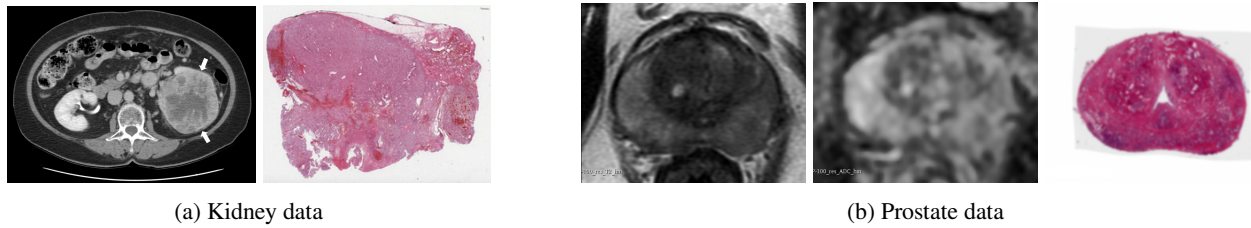


Figure 1: Example images for kidney and prostate data. (a) CT image (left) with an aggressive tumor highlighted with arrows, and the histopathology slice (right) showing a surgically resected tissue at an unknown location from the tumor. Please note the differences in resolution. (b) Spatially aligned T2w, ADC and histopathology images from the prostate cohort.

learning these radiology-pathology correlations and in identifying pathology-informed radiology biomarkers for classification of clear cell RCC using radiology images alone.

Prior machine-learning based image-analysis methods for RCC focused on differentiating between malignant or benign masses (Coy et al., 2019; Sun et al., 2020; Tanaka et al., 2020), classifying histological subtypes (Yan et al., 2015; Han et al., 2019; Zuo et al., 2021; Uhm et al., 2021), or distinguishing between low- and high-grade clear cell RCC (Ding et al., 2018; Kocak et al., 2019; Bektas et al., 2019; Lin et al., 2019; Sun et al., 2019; Shu et al., 2019; Nazari et al., 2020; Cui et al., 2020; Lin et al., 2020; Xv et al., 2021; Demirjian et al., 2021). In this study, we extend the definition of aggressiveness to include both tumor grade and presence of necrosis, as multivariate analysis gives better prognostic value (Hötter et al., 2016; Tse et al., 2021). No prior study attempted to classify clear cell RCC as aggressive or indolent using machine learning, based on both tumor grade and necrosis observed on pathology images.

Only one study considered complementary histopathology images and genetic data in addition to radiology images for prediction of prognosis in clear cell RCC (Ning et al., 2020). The study showed that the multi-domain approach has the best performance, suggesting the benefit of multi-modal data fusion. Yet, the requirement for all three modalities to be available as input data limits the clinical relevance of this approach, since both histological and genetic data may not be available in the pre-operative setting.

Methods incorporating histopathology information during model training, while not requiring it during inference have been described for prostate cancer (Bhattacharya et al., 2020, 2022b), but to our knowledge have not been developed for kidney cancer. The radiology-pathology fusion approach developed for the prostate can detect and differentiate between indolent and aggressive prostate cancer on Magnetic Resonance Imaging (MRI) (Bhattacharya et al., 2022b). It is able to emphasize disease pathology characteristics on MR images by learning MRI features that are correlated with histopathology features on a per-pixel level. Thus, the method relies on registered (spatially aligned) MRI and histopathology images for creating these pathology-correlated radiology image biomarkers. The study showed that including MRI biomarkers improved the performance of prostate cancer detection over MR images alone.

Inspired by this prior study, we developed an approach

to learn and use CT features in the kidney that correlate with histopathology image features for classification of clear cell RCC aggressiveness. However, application of the prior prostate approach to other cancer types is complicated by the dependence on spatially aligned radiology and pathology data, something usually lacking in datasets from other organ systems. In addition to the lack of registered radiology and pathology data, the clear cell RCC aggressiveness prediction task differs from the prostate task in the use of a different radiology imaging modality (CT vs. MRI), different organ (kidney vs. prostate) with different tissue characteristics in the histopathology images, and a different prediction challenge (classification vs. segmentation) (Figure 1).

To enable accurate aggressiveness prediction of clear cell RCC on CT images, we present a novel radiology-pathology fusion approach, Correlated Feature Aggregation By Region (*CorrFABR*), that identifies and uses radiology features that are correlated with disease pathology characteristics observed in resected tissue. Unlike the prior prostate study (Bhattacharya et al., 2022b), *CorrFABR* does not require spatial alignment between radiology and pathology images. *CorrFABR* also includes a novel feature extraction module enabling feature aggregation from radiology and histopathology images at different resolutions.

Our study has two parts. First, starting from a clinical dataset with existing spatial correspondences, *CorrFABR* is developed and trained on simulated prostate biopsy and surgery datasets *without* pixel-wise spatial correspondences between the radiology and pathology images. Second, using public data without spatial correspondences, *CorrFABR* is trained and evaluated on cohorts from the 2021 Kidney Tumor Segmentation Challenge (Heller et al., 2021) and The Cancer Imaging Archive (TCIA) (Clark et al., 2013) to predict the aggressiveness of clear cell RCC.

The main contributions of this paper, which are encompassed by the proposed *CorrFABR* method, can be summarized as:

1. Development of radiology image biomarkers that correlate with pathology features without spatial alignment of the data through feature aggregation by region.
2. Presentation of a novel approach for handling feature aggregation between radiology and pathology images with widely different resolutions.

Table 1

Dataset summary of the prostate and kidney cohorts. Available annotations of cancerous regions were either done manually by trained clinicians or automatically using pre-trained machine learning methods.

	Prostate						Kidney		
	P_{cancer} : Radical Prostatectomy			P_{normal} : Normal			KiTS21	TCGA-KIRC	
Number of Patients	115			24			203	174	
Sex (male/female)	115 / 0			24 / 0			133 / 70	110 / 64	
Registered	Yes			N/A			N/A	No	
Data	MRI		Hist.	MRI		CT	CT	Hist.	
Sequence/Data Type	T2w	ADC	H&E	T2w	ADC	Enhanced	Enhanced	H&E	
Number of slices (per volume)	4–11	4–11	4–11	6–22	6–22	29–1059	32–306	1	
In-plane resolution (mm)	0.27–0.94	0.78–1.50	0.008–0.016	0.35–0.43	0.78–1.25	0.59–1.04	0.50–0.98	$[0.25 - 0.5] \cdot 10^{-3}$	
Distance between slices (mm)	3.0–5.2	3.0–5.2	3.0–5.2	3.0–4.2	3.0–4.2	0.5–5.0	1.25–7.5	N/A	
Annotation type	Manual	Manual	Automatic	Manual	Manual	Manual	Automatic	Not available	

3. Demonstrate the application for indolent and aggressive characterization in clear cell RCC.

The rest of the paper is organized as follows: the datasets used are presented in Section 2.1, followed by a description of the proposed method in Section 2.2. Section 3 describes the experimental setup and presents results. In Section 4, the method and results are discussed.

2. Material and methods

2.1. Dataset

This work considers two different urologic cancer types: prostate cancer and renal (kidney) cancer.

2.1.1. Cohort Used for Simulated Prostate Data

First, we used clinical prostate data (described below) to simulate lack of spatial alignment between radiology and pathology images. The clinical prostate dataset consists of two subcohorts (Table 1): (a) P_{cancer} (N=115) includes men who had confirmed prostate cancer and underwent radical prostatectomy, and (b) P_{normal} (N=24), includes men without prostate cancer confirmed by negative MRI and negative biopsy. All men underwent multi-parametric Magnetic Resonance Imaging (MRI) prior to the biopsy or surgery. Our study included the T2-weighted (T2w) sequence and the Apparent Diffusion Coefficient (ADC) maps. For the patients in P_{cancer} , the resected tissue was sectioned in the same axial plane as the MR-sequence using a patient-specific 3D mold. The tissue was fixed and stained with Hematoxylin & Eosin (H&E)-staining and scanned at 20x magnification. The digitized histopathology images were then registered to the corresponding pre-operative MRI slices using the RAP-SODI registration platform (Rusu et al., 2020), resulting in spatially aligned radiology and pathology images on a slice-level (Figure 1b). The Internal Review Board at Stanford University approved the retrospective study with waived patient consent. For more information about the cohort, and details on data processing and registration, please see (Bhattacharya et al., 2022b,a).

Labels and annotations Each patient in the P_{cancer} cohort had annotations showing either normal tissue, indolent (Gleason Grade Group = 1) or aggressive (Gleason Grade Group > 1) cancer, as well as the prostate gland outlined. On radiology, the annotations were outlined by a radiologist and confirmed by pathology findings. The annotations on the histopathology data were created automatically using a previously validated deep learning model (Ryu et al., 2019), and processed using morphological processing and connected component analysis to ensure lesions were continuous in 3D. Lesions smaller than 250mm^3 were discarded as these are less likely to be seen on MRI and less likely to be clinically significant cancer (Matoso and Epstein, 2019). For more information about the annotation process, see Bhattacharya et al. (2022a).

The strategy used to create the simulated prostate data is described below in Section 2.2.

2.1.2. Kidney Cohort

For renal cell carcinoma, we used publicly available clinical data from the 2021 Kidney and Kidney Tumor Segmentation Challenge (KiTS21) and The Cancer Imaging Archive (TCIA): TCGA-KIRC. All patients included in this study had confirmed clear cell RCC, underwent contrast-enhanced CT scans, and, in the case of TCGA-KIRC, had corresponding diagnostic histopathology images from partial or radical nephrectomy. This resulted in 203 patients with CT from the KiTS21 dataset (Heller et al., 2021), and 174 patients with CT and histopathology from the TCGA-KIRC cohort (Akin et al., 2016) (Table 1). The tumor diameter (mean and standard deviation (SD)) was 5.01 (SD=3.11) cm for KiTS21 and 5.83 (SD=2.89) cm for TCGA-KIRC (see Table S2 for details). Figure 1a shows example data from a sample patient in the kidney cohort.

Labels and annotations The KiTS21 data included manually segmented regions of the kidneys and tumors. For the TCGA-KIRC data, no manual segmentations were available. Automatic segmentations of the kidneys and tumors were extracted on CT using the previously validated and pre-trained MIScnn model (Müller and Kramer, 2021). These segmen-

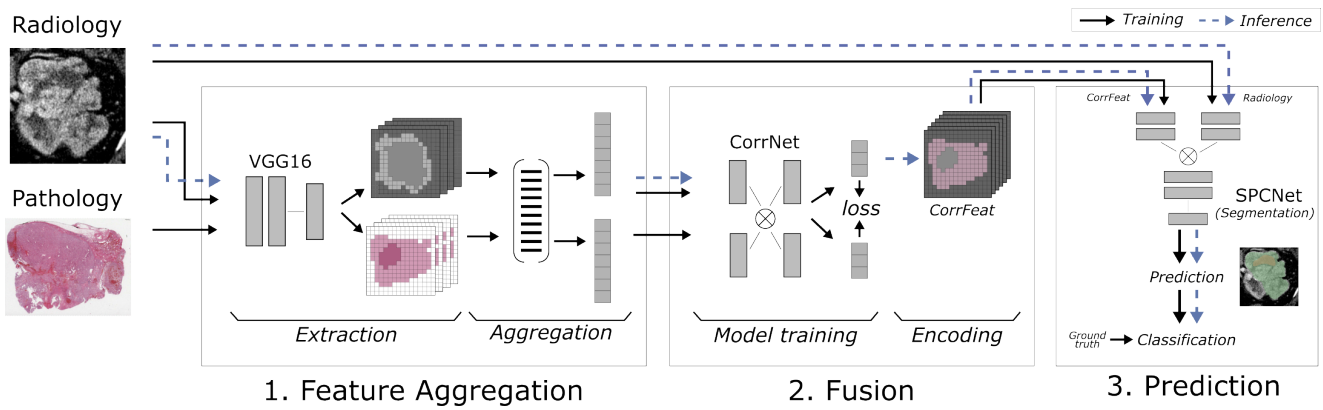


Figure 2: Summary of the proposed method *CorrFABR*. The three-step approach consists of a feature aggregation step, a fusion step between the radiology and pathology data, and finally, incorporation of fused radiological image biomarkers to a prediction model, of which the output can be classification or segmentation map. During training, the radiology image(s), and the pathology image, are used in steps 1 and 2. The model trained in step 2 is applied to the radiology images, creating *correlated features*, denoted *CorrFeat*. These, together with the radiology data, are used as model input in step 3. During inference (blue dashed track), pathology images are not needed.

tations were visually inspected for quality assurance. On histopathology data, tissue was segmented from background using Otsu thresholding (Otsu, 1979).

Each tumor was labeled as either indolent or aggressive using the pathology reports. Aggressive tumors were defined as having necrosis or a high tumor grade (Fuhrman (Fuhrman et al., 1982) or ISUP (International Society of Urological Pathology) (Moch et al., 2016) grade of 3 or 4). Indolent tumors were defined as those with low tumor grade (1-2) without necrosis (Bhindi et al., 2018). Tumor grade and necrosis were both included in the definition of aggressiveness, since both are considered important prognostic markers for clear cell RCC (Fuhrman et al., 1982; Beddy et al., 2014; Tse et al., 2021; Zigeuner et al., 2010). Out of the total 372 tumors, 199 were labeled as aggressive. 19 low-grade (grade 2) cases had presence of necrosis (see Table S3 for details), thus considered aggressive despite low tumor grade. While clear cell RCC tumors may be heterogeneous, with both low- and high-grade areas, the lack of pixel-wise annotations restricted labels with finer granularity. Thus, the lesion segmentation masks were created by setting all values in the segmented lesion to the corresponding class.

Pre-processing All CT volumes were cropped using a three-dimensional bounding box extracted from the lesion segmentations and resized to an in-plane dimension of 224x224 pixels. By using the intensity values inside the lesion, each cropped volume was Z-score normalized. Due to the variability of stain color in the public data, the histopathology images were stain normalized by the method from Macenko et al. (2009). For low-resolution feature extraction (described in Section 2.2), the data were downsampled to an image size of 224x224 pixels.

2.2. Method

This study aims to present a method for incorporating disease characteristics from histopathology images in to the radiology domain without requiring spatial alignment between the two domains. The overarching goal is to enable improved prediction performance using radiology images alone during inference. An overview of the proposed method, Correlated Feature Aggregation By Region (CorrFABR), is shown in Figure 2, which consists of three steps:

1. Feature extraction and aggregation from radiology and pathology images
2. Fusion to learn a combination of radiology features that correlate with pathology features (denoted *CorrFeat*)
3. Prediction to classify clear cell RCC tumors as aggressive or indolent, using either the correlated features alone (*CorrFeat*), or together with the radiology images.

During training, unaligned radiology and pathology images originating from the same patient are used in Step 1 (Feature aggregation) and Step 2 (Fusion). For training of the model in the Step 3 (Prediction), as well as during inference, only radiology images are needed. Therefore, the model only relies on histopathology data during the training phase of two out of three steps, and never during inference. Below, each step of the method is described in more detail.

2.2.1. Input data

During training, for each patient, image data from the radiology and pathology domains are used. In this work, we consider 3-dimensional radiology data (MRI or CT) where each slice containing the lesion is considered separately. Each slice is paired with a whole-slide image (WSI) from the histopathology domain. A pair formed by one radiology slice and one WSI are used as input to Step 1, Feature aggregation.

2.2.2. Feature aggregation

The first step of the method extracts feature vectors from the input images, which will be used as input to the fusion model in Step 2. Feature extraction was done using the first two layers of a pre-trained VGG16 model (Bhattacharya et al., 2022b). Image sizes of 224x224 pixels were used for radiology images, resulting in feature maps of shape [224, 224, 64], where 64 is the number of filter outputs from the second VGG16 layer (Simonyan and Zisserman, 2015). For histopathology data, two approaches were evaluated. The first approach, denoted *low-res*, assumes downsampled and resized data of size 224x224 pixels, giving feature maps of shape [224, 224, 64]. The second approach, denoted *high-res*, extracts features at a higher resolution (between 0.008 – 0.032 mm/pixel) in a patch-wise manner, with a patch size of 224x224 pixels. The number of patches per image depends on the width and height of the WSI. For each patch, the features are averaged, resulting in a 1x64 vector *per patch*. Depending on the width (w) and height (h) of the input image, the feature maps are of shape $[w/224, h/224, 64]$.

The extracted radiology and pathology features are then aggregated for fusion using three scenarios as below:

(a) *Pixel-pixel fusion* (Figure 3 (a)): This feature aggregation applies to the scenario where the radiology and pathology images are spatially aligned, enabling pixel-level fusion, as used in (Bhattacharya et al., 2022b). The aggregation of the features is done by flattening in the in-plane dimension, such that each corresponding pixel between the two domains, radiology and pathology, is considered an input-vector pair to the fusion model. Only *low-res* aggregation is possible for this scenario, as it assumes the same resolution for both domains. Per patient, the set $S_{pixel} = \{S_{rad}, S_{pat}\}$ was formed, with sizes $S_{rad} = [224 \times 224, 64 \times n]$ and $S_{pat} = [224 \times 224, 64]$, where n denotes the number of input sequences available. In the case of the prostate cohort, $n = 2$ (T2w and ADC), and for kidney $n = 1$ (CT). Following (Bhattacharya et al., 2022b), the number of input vectors was class balanced between cancer and non-cancer vectors, and limited to 1 million inputs per training set.

(b) *Lesion-TMA/biopsy fusion* (Figure 3 (b)): This feature aggregation is for the targeted biopsy scenario, where a small tissue microarray (TMA) is extracted from the targeted lesion. Typically, the TMA section is small, and may contain a mixture of cancerous tissue from the lesion and normal tissue from adjoining regions.

In this scenario, the features were considered on a per-lesion basis instead of on a per-pixel basis. Feature values within the lesion regions were aggregated into one value in the in-plane dimension on a per-lesion basis in the radiology domain and per-TMA section basis in the pathology domain. For the extracted *low-res* histopathology features, aggregation was done by simply taking the average. For the extracted *high-res* histopathology features, the features were aggregated across the region by taking the 95th percentile of the intensity values. This approach ensures that local,

high-resolution information is captured in the patches, and the aggregation over the region using the top percentile ensures that high, local, feature responses are maintained.

In addition, normal tissue patches were extracted from randomly selected normal areas of $\approx 0.5 \times 0.5$ cm (20x20 pixels in *low-res*).

Per patient, the set $S_{biopsy} = \{S_{rad}, S_{pat}\}$ is now constructed by j number of lesion regions and k number of normal regions, with the size $S_{rad} = [(j + k), 64 \times n]$ and $S_{pat} = [(j + k), 64]$.

(c) *Lesion-section fusion* (Figure 3 (c)): This feature aggregation is for scenarios where the entire lesion has been removed via surgery. The histopathology image consists of a large section of tissue containing cancerous tissue together with some adjacent normal tissue. In contrast to the TMA/biopsy scenario, the region is now larger, may be more heterogeneous, and may contain larger portions of normal tissue. Feature aggregation for this scenario was conducted similarly to lesion-TMA/biopsy scenario (b). Thus, per patient, we now have set $S_{section} = \{S_{rad}, S_{pat}\}$ constructed by j number of lesion regions and k number of normal regions, with the size $S_{rad} = [(j + k), 64 \times n]$ and $S_{pat} = [(j + k), 64]$.

2.2.3. Fusion

The fusion step enables learning radiology biomarkers that are correlated with pathology features. It consists of two parts: model training and encoding. The model considered in this work is a Correlational Neural Network (CorrNet) (Chandar et al., 2016). CorrNet learns a common representation between two input vectors, such that they are maximally correlated in this lower dimensional latent space, while at the same time minimizing the reconstruction error between the output of the decoder and input. The reconstruction loss prevents collapse of the latent representation (e.g., all zeros).

The CorrNet model architecture consists of one encoder-decoder pair for each input domain (see Figure 4). Using one vector pair from S (where S is either S_{pixel} , S_{biopsy} or $S_{section}$ from Step 1), the input vectors R_i and P_i are constructed, originating from radiology and pathology data respectively. The latent representations $h_R = f(W R_i + b)$ and $h_P = f(V P_i + b)$ are the output from the single-layer encoders of each domain, respectively. f can be any linear or non-linear function, and $W \in \mathbb{R}^{k \times 64 \times n}$, $V \in \mathbb{R}^{k \times 64}$ and $b \in \mathbb{R}^{k \times 1}$, where k is the size of the latent representation and n denotes the number of input sequences available. The joint hidden representation is given by

$$h(R_i, P_i) = f(W R_i + V P_i + b). \quad (1)$$

The loss consists of two parts. The first part, denoted L_{recon} , minimizes the reconstruction of the between the input and the output of the decoder ($R'_i = g(W' h_R + b')$ and $P'_i = g(V' h_P + b')$, g is any activation function.). The second part, denoted L_{corr} , maximizes the correlation between h_R and h_P . The total loss is therefore:

Correlated Feature Aggregation by Region

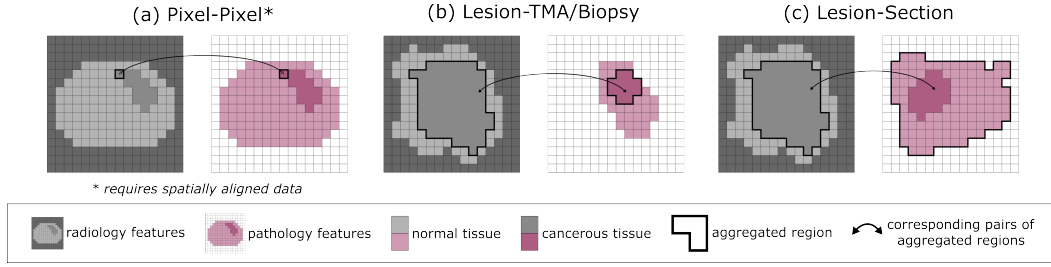


Figure 3: Schematic overview of the three different aggregation methods for creating paired feature vectors between radiology and pathology feature responses. For (b) and (c), pathology feature extraction can be done in both low- and high-resolution. (a) Pixel-pixel: feature vectors at each pixel position (requires spatially aligned data). (b) Lesion-TMA/biopsy: smaller cutouts of selected tissue from the histopathology domain together with that lesion region from radiology. (c) Lesion-section: larger cutouts of tissue from the histopathology domain together with that lesion region in radiology. Figure best viewed in color.

$$L = L_{recon} + \lambda L_{corr}, \quad (2)$$

where L_{recon} is given by

$$L_{recon} = \sum_{i=1}^N (L(R_i, R'_i) + L(P_i, P'_i)) \quad (3)$$

and N is the number of samples in one batch and L is the reconstruction error calculated using mean squared error. L_{corr} is given by

$$L_{corr} = \frac{\sum_{i=1}^N (h_R^i - \bar{h}_R) (h_P^i - \bar{h}_P)}{\sqrt{\sum_{i=1}^N (h_R^i - \bar{h}_R)^2 (h_P^i - \bar{h}_P)^2}}. \quad (4)$$

In this study, $\lambda = 2$ for all experiments, the dimension of the hidden space was set to $k = 5$, and f and g are set as the identity function (Bhattacharya et al., 2020).

Once the model is trained, only the encoder part of the radiology domain is used, applied to radiology data alone. This ensures that the method is usable for clinical inference, where the pathology data is unavailable. For inference, the input radiology features are flattened in the in-plane dimension. The output of the encoder, h_R have size $[224 \times 224, 5]$,

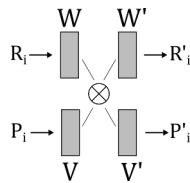


Figure 4: CorrNet model, with R_i and P_i as input representing one pair of feature vector. The input is processed through the single-layer encoder with weights W and V , respectively. The correlation loss (L_{corr}) forces the resulting representations to be as correlated as possible. The output from the single-layer decoders, W' and V' , reconstructs the input signal as closely as possible through the reconstruction loss (L_{recon}).

Table 2

Number of unique cases in training and test splits for different tasks.

Task	E1: Prostate Pixel-level agg.			E2: Kidney Tumor-level agg.		
	P_{cancer}	P_{normal}	Total	Indolent	Aggressive	Total
Train	75	24	99	136	162	298
Test	40	0	40	37	37	74

is reformatted as $[224, 224, 5]$, forming image-shaped features henceforth denoted $CorrFeat$. These are the maximally correlated features between the radiology and pathology domain, constructed without pathology data and used as input to the third and final step, prediction.

2.2.4. Prediction

The SPCNet (Seetharaman et al., 2021) architecture was used as prediction model, taking both radiology input as well as correlated features ($CorrFeat$) created from Step 2, outputting a segmentation mask. The architecture of SPCNet is based on the holistically nested edge detector (HED) (Xie and Tu, 2017). SPCNet inputs three adjacent slices from the input radiology volume to predict the segmentation output of the center slice. One (1) or multiple sequences/inputs are inputted by separate branches consisting of convolutional layers, concatenated to form the segmentation output. In this work, we consider different scenarios depending on the available data. For prostate, the input radiology consists of two sequences, T2w and ADC. The SPCNet architecture has with this input two branches (denoted MRI). In addition, a third input can be added for the $CorrFeat$, resulting in three branches (denoted $MRI + CorrFeat$). For the kidney data, the input radiology consists of one CT volume, resulting in SPCNet architecture of one (1) branch (denoted CT). When the $CorrFeat$ are added, the number of branches is extended to two (denoted $CT + CorrFeat$). In addition, for both prostate and kidney, the case where only the $CorrFeat$ are used as input is evaluated (one branch).

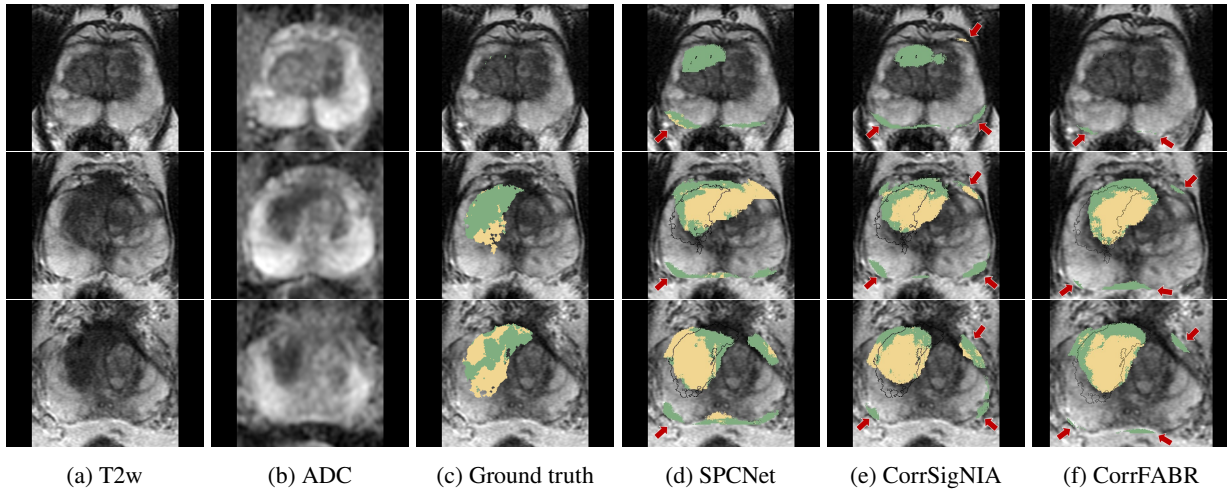


Figure 5: Three slices from one patient from the prostate test cohort with an aggressive tumor in the anterior and central part of the prostate. The three left-most panels show T2w, ADC, and T2w with ground truth segmentations overlaid (indolent regions in green, aggressive in yellow). The right-most panels show prediction results for (d) SPCNet (no CorrFeat), (e) CorrSigNIA (pixel-pixel CorrFeat), and (f) CorrFABR (lesion-section CorrFeat), with ground truth overlaid (black outline). Arrows show examples of false positive predictions.

Table 3

Lesion-wise results for aggressive prostate cancer detection on MRI (Experiment E1). Qualitative results for SPCNet, CorrSigNIA, and CorrFABR with lesion-section aggregation from high-resolution pathology are visualized in Figure 5.

Method	Pathology Resolution	Spatial Alignment	Feat. Aggregation	Input Rad.	Input CorrFeat	ROC-AUC	Dice	Sensitivity	Specificity
SPCNet	N/A	N/A	None	✓	-	0.86 ± 0.28	0.36 ± 0.19	0.86 ± 0.34	0.48 ± 0.35
CorrSigNIA	Low	✓	Pixel-pixel	✓	✓	0.87 ± 0.29	0.37 ± 0.21	0.86 ± 0.34	0.60 ± 0.37
CorrFABR	Low	-	Lesion-TMA/biopsy	✓	✓	0.89 ± 0.27	0.36 ± 0.21	0.82 ± 0.37	0.53 ± 0.36
CorrFABR (visualized)	Low	-	Lesion-section	✓	✓	0.90 ± 0.22	0.36 ± 0.19	0.94 ± 0.22	0.51 ± 0.37
CorrFABR	High	-	Lesion-section	✓	✓	0.87 ± 0.31	0.36 ± 0.22	0.86 ± 0.34	0.59 ± 0.37
CorrFABR	High	-	Lesion-section	-	✓	0.84 ± 0.30	0.32 ± 0.21	0.82 ± 0.38	0.49 ± 0.34

3. Experiments and results

We use two experimental setups to train and evaluate CorrFABR. In the first experiment, data from prostate cancer patients with existing spatial correspondences between radiology and histopathology images are used. The alignment is synthetically removed to simulate more common data-availability scenarios originating from targeted biopsy or surgery. We train CorrFABR to learn correlated MRI features in this simulated prostate scenario, with the goal of selectively identifying aggressive and indolent prostate cancer on MRI. In the second experiment, we train and evaluate CorrFABR to classify clear cell RCC lesions as aggressive and indolent using CT images from publicly available data. In both scenarios, there is no spatial alignment or slice-to-slice correspondence between the radiology and pathology images.

3.1. Experiment 1 (E1): Prostate

In this experiment, we synthetically modify the unique spatially aligned data to simulate “real-world” data for the prostate, where (a) pathology images are acquired either through biopsy or after surgery, and (b) exact registration or spatial correspondence between radiology and pathology images is unknown. The goal of this experiment was not to improve performance over previous methods for prostate lesion

segmentation, but to enable development and assessment of radiology-pathology fusion models in simulated prostate scenarios when spatial alignment is unavailable. Another goal was to increase understanding of how to modify the fusion approaches for renal cell carcinoma, where only a rough estimate of the location of the pathology image is known. This is in contrast to previously presented radiology-pathology fusion methods (Bhattacharya et al., 2020, 2022b), which relied on both in-plane spatial alignment, as well as slice-to-slice correspondence between the radiology and pathology images.

3.1.1. Dataset

Two different aggregation scenarios were considered (see Section 2.2 and Figure 3): lesion-TMA/biopsy (simulating targeted biopsy) and lesion-section (simulating surgery). In the radiology domain, for both scenarios, lesion-level T2w and ADC features were extracted and aggregated from regions within the lesion outline on a per-slice basis, resulting in one aggregated feature vector per lesion of size 1×128 . Features were also aggregated from normal regions by randomly sampling the same number of normal patches as lesion vectors from a single patient.

In the pathology domain, smaller and larger regions were

extracted using lesion annotations to simulate real-world biopsy and surgery scenarios. The selected histopathology sections were randomly offset beyond the lesion outlines to include some random fraction of normal tissue in addition to a minimum threshold of cancerous tissue. To further simulate the biopsy and surgery scenario, *high-res* features were extracted from pathology (as described in Section 2.2).

Feature vectors from the histopathology images are paired with the corresponding lesion in radiology, but from a randomly selected slice. Feature vectors from normal regions are similarly paired with vectors from normal regions, but from randomly selected slices and locations.

As an intermediate step, the method was evaluated in the case where spatial alignment was kept, but features were aggregated on a per-region basis. Results for this experiment is shown in the Supplementary Material.

3.1.2. Training and test set split

For the prostate cohorts, 99 patients from P_{cancer} and P_{normal} cohorts were used for training, and 40 cases from P_{cancer} were used for independent testing (Table 2). As only cases from P_{cancer} had corresponding histopathology, these cases were used in Step 1 and 2 of training (feature extraction, aggregation, and training of the fusion model, described in Section 2.2), but all cases were used for Step 3 (prediction) of training.

The models were trained in a 5-fold cross-validation setting, by splitting the 99 cases in training into five equally sized groups, such that each group had 20 (or 19) unique cases. For each group, a model was trained on all cases not included, and the remaining cases were used to validate the model. The folds were kept fixed during all three steps of the method. The final segmentation outputs of the five models were averaged to form one final prediction segmentation, from which the evaluation metrics were calculated.

3.1.3. Training details and evaluation

Two models were considered baseline: the SPCNet model with only radiology images as input (Seetharaman et al., 2021), and the prior method from Bhattacharya et al. (2022b), *CorrSigNIA*, which used MRI + *CorrFeat* as input, where *CorrFeat* was learned using pixel-pixel feature aggregation and fusion.

For Step 2, the CorrNet models were trained for 1000 epochs, with learning rate $0.5 \cdot 10^{-4}$ and batch size 50. For Step 3, the SPCNet models were trained for maximally 100 epochs, a learning rate of 0.001, and batch size of 8. The learning rate was reduced by 0.1 if the validation loss had not been reduced in 10 epochs. Early stopping was used with a patience of 20 epochs, and the final model was used for evaluation.

The prediction model was trained to selectively identify normal tissue, indolent cancer, and aggressive cancer on the entire prostate. The models were evaluated in detecting and localizing aggressive prostate cancer on MRI using a sextant-based approach used in previous studies (Seetharaman et al., 2021; Bhattacharya et al., 2022b,a). Models using MRI-only (baseline), MRI + *CorrFeat*, as well as *Corr*

rFeat only were evaluated. ROC-AUC, Dice, sensitivity, and specificity are reported for detection of lesion-level aggressive cancer (see below).

3.1.4. Results

Qualitatively, both CorrSigNIA and CorrFABR resulted in fewer false-positive regions identified compared to the baseline SPCNet method that did not incorporate any correlated features (Figure 5). Furthermore, there is less over-segmentation using the CorrFABR method, especially notable in the top slice. Please see Figure S1 for qualitative results in another patient.

Quantitatively, CorrFABR demonstrated better or similar performance compared to the baseline CorrSigNIA approach, despite lacking spatial alignment between the radiology and pathology images (Table 3). Comparing the high-resolution and low-resolution approaches for feature extraction from the histopathology data, the Dice score is nearly identical. This suggests that the extraction of histopathology features at high resolution is not needed. The ROC-AUC and sensitivity were higher for the low-resolution case, but at the cost to a lower specificity. CorrFABR with low-resolution and lesion-section aggregation resulted in higher ROC-AUC, sensitivity and specificity, and similar Dice compared to baseline. Using only *CorrFeat* as input, without MRI gave a slightly lower result in terms of ROC-AUC, Dice, and sensitivity (bottom row), indicating the need for the structural information present in the MRI data. Overall, the results show the benefit of using correlated registration learning in the real-world scenario where perfect registration is not available between radiology and pathology images.

3.2. Experiment 2 (E2): clear cell renal cell carcinoma aggressiveness prediction

In this experiment, the approach described in E1 was adapted to train models on the kidney cohort for clear cell RCC tumor aggressiveness prediction. This cohort naturally lacks both pixel-level and slice-level correspondence, and the histopathology data consist of a single slice per patient, with a section of the surgically removed tissue used for diagnosis (see Figure 1a).

3.2.1. Dataset

The lesion-section feature aggregation was used for this task, as the histopathology images were from surgically removed sections of the lesion with no spatial alignment with the radiology images. Moreover, the histopathology images lacked cancer annotations. Feature extraction of the pathology features was evaluated both for the *low-res* and the *high-res* approach.

For each slice in the 3-dimensional CT volume, the features were extracted and aggregated from the annotated lesion region, similar to methods used for the prostate. For the histopathology data, only one whole-slide pathology image was available per patient. Due to lack of annotations, no normal regions were extracted. The feature vector extracted and aggregated from the entire tissue section (from either low- or

Table 4

Lesion-wise results for clear cell RCC tumor aggressiveness classification (Experiment E2). Quantitative results for SPCNet and CorrFABR with lesion-section aggregation from high resolution pathology (*CorrFeat* only) are visualized in Figure 6.

Method	Pathology Resolution	Spatial Alignment	Feat. Aggregation	Input Rad.	Input <i>CorrFeat</i>	ROC-AUC	F1-score	Sensitivity	Specificity
VGG16	N/A	N/A	None	✓	-	0.78 ± 0.03	0.68 ± 0.04	0.62 ± 0.16	0.76 ± 0.13
SPCNet	N/A	N/A	None	✓	-	0.72 ± 0.05	0.66 ± 0.02	0.49 ± 0.07	0.85 ± 0.04
CorrFABR	Low	-	Lesion-section	✓	✓	0.74 ± 0.04	0.68 ± 0.06	0.63 ± 0.10	0.75 ± 0.13
CorrFABR	High	-	Lesion-section	✓	✓	0.75 ± 0.03	0.67 ± 0.04	0.58 ± 0.12	0.77 ± 0.17
CorrFABR (<i>visualized</i>)	High	-	Lesion-section	-	✓	0.78 ± 0.02	0.73 ± 0.03	0.64 ± 0.08	0.83 ± 0.06

high-resolution images) was paired with each of the slices in CT volume.

3.2.2. Training and test set split

A total of 378 cases were included from KiTS21 and TCGA-KIRC. A test set of 74 cases with balanced distribution of aggressive and indolent clear cell RCC was randomly selected from KiTS21, to ensure that the test set included cases of high segmentation quality. The remaining cases not included in the test set formed a 5-fold cross-validation setup (Table 2). As only TCGA-KIRC included CT and histopathology data, this cohort was used to train in steps 1 and 2, while training cases from KiTS21 were included in Step 3. The evaluation metrics are reported as mean and standard deviation between models and folds on a per-lesion level.

3.2.3. Training details and evaluation

For incorporation of the *CorrFeat*, the SPCNet model was used, evaluated on both CT + *CorrFeat*, and *CorrFeat* only. A five-fold cross-validation approach was used with the same training hyperparameters as used for experiment E1, for both the CorrNet model and the SPCNet model. As a baseline prediction model, a VGG16 model was evaluated using CT data only. Using transfer learning from pre-trained ImageNet weights, the model was trained similarly with early stopping, a learning rate of 0.001, and batch size of 8. To avoid overfitting, only the last layer was fine-tuned. While model weights are available from the prostate Experiment E1, they were not used as part of Experiment E2 due to the different nature of the input data and pathology appearance.

For the kidney task, the goal was to discriminate between indolent or aggressive cancer on a per-lesion basis. As the SPCNet model was trained for a segmentation endpoint, the output segmentation volumes were converted to binary class labels on a per-patient level by setting the predicted class as the one with the largest number of predicted pixels. The reported metrics are ROC-AUC, F1-score, sensitivity, and specificity (see below).

3.2.4. Results

This experiment evaluates the method on data where there is only a patient-level correspondence between the radiology and pathology data and no spatial alignment between the images.

From qualitative inspection of the segmentation outputs,

we see that the incorporation of pathology-correlated radiology image biomarkers (proposed method) helps to better discriminate the aggressive and indolent tissue characteristics on CT images by labeling more pixels as the correct class (Figure 6). Especially in one of the aggressive cases (middle), the CorrFABR method correctly classifies large portions in the center of the tumor, which the SPCNet model misclassified as indolent regions.

Quantitatively, comparing baseline methods of VGG (pre-trained on ImageNet) and SPCNet that neither incorporate correlated data from histopathology gave similar performance as to adding the correlated features together with CT data (Table 4). However, when the correlated features were used stand-alone using high-resolution histopathology features (bottom row), the F1-score improved from 0.68 ± 0.04 and 0.66 ± 0.02 respectively to 0.73 ± 0.03 . Furthermore, both low- and high-resolution approaches gave similar results, indicating the feasibility of using either approach for correlated feature training by region.

4. Discussion

We presented a novel method, CorrFABR (Correlated Feature Aggregation By Region), for incorporation of disease characteristics from histopathology images to help in radiologic assessment without the need for spatially aligned radiology and pathology images. By extending previous approaches (Bhattacharya et al., 2020, 2022b), the proposed method creates correlated features from aggregated regions from each image domain, removing the need for pixel-to-pixel aligned data. Starting from spatially aligned radiology and pathology prostate images, we synthetically remove the pixel- and slice correspondence to mimic the more common data-availability scenario. Despite this, it is still possible to extract valuable correlated information that improves prostate cancer detection over MRI features alone (Table 3), even better than when pixel-to-pixel correlation are used. This benefit can be attributed to the fact that even when pixel-to-pixel correspondences are assigned, registration errors exist. In the case of the prostate, they are estimated to be between 2-3mm (Rusu et al., 2020). By doing region-based correlation learning, the effect of the registration error is reduced. This motivated us to apply the approach to the more challenging real-world data of clear cell renal cell carcinoma (RCC).

Accordingly, the method was evaluated on public CT data for tumor aggressiveness classification of clear cell RCC.

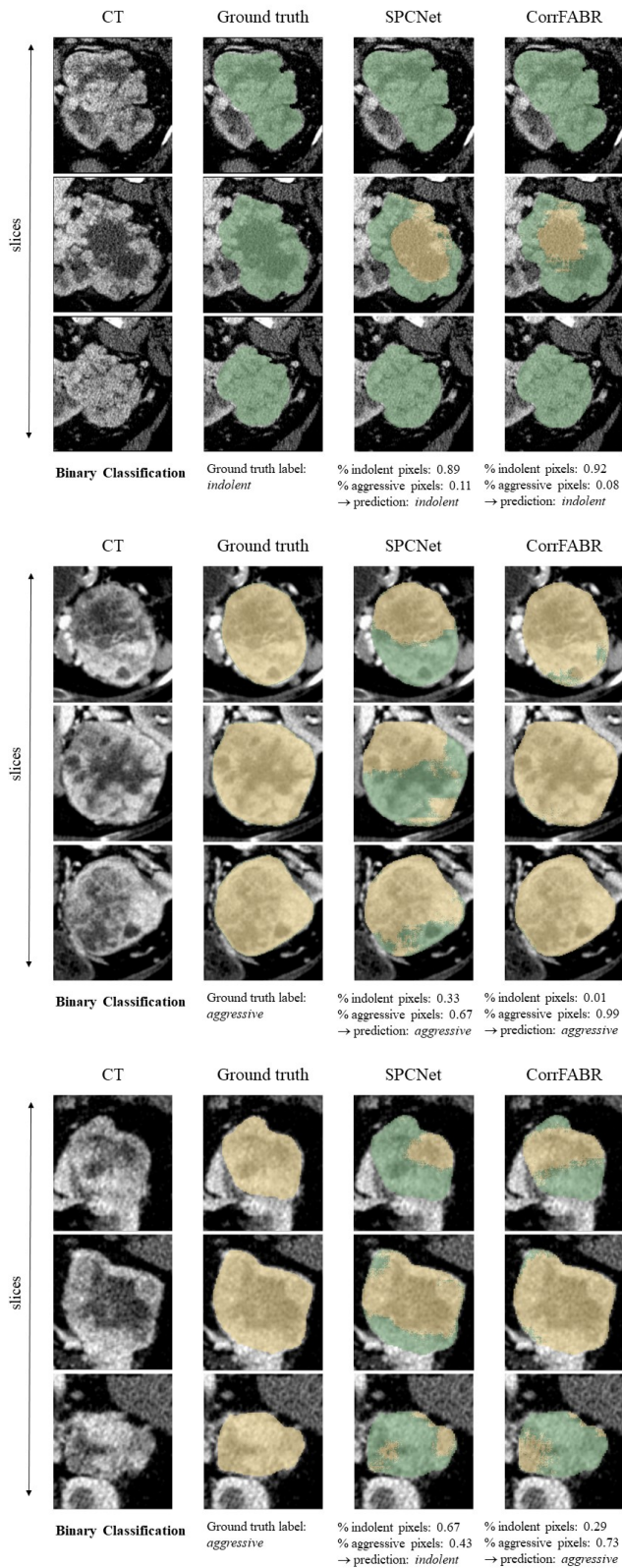


Figure 6: Results for clear cell classification, showing three slices from three different cases. Green denote indolent pixels, yellow aggressive. The segmentation values are converted to binary classification by majority vote. Best viewed in color.

By using both high tumor grade (grade 3 or 4) as well as the presence of necrosis as definition of aggressiveness, we incorporated two important prognostic factors (Minardi et al., 2005; Hötker et al., 2016; Rabjerg et al., 2021).

Previous methods have been presented for tumor-grade classification only, without reference to necrosis (Ding et al., 2018; Kocak et al., 2019; Bektas et al., 2019; Lin et al., 2019; Sun et al., 2019; Shu et al., 2019; Cui et al., 2020; Lin et al., 2020; Xv et al., 2021; Demirjian et al., 2021). Therefore, numerical comparison of results is challenging, as the target endpoint is different. This is further amplified by evaluation on internal data only and/or the use of different/multiple input data sequences (unenanced, varying delay times of enanced images, or multiple phases).

Comparing the results from the first experiment of simulated prostate data with the second experiment of real-world kidney data, we see that the method generalized to (a) a different disease beyond the prostate, (b) a different radiology image (CT vs. MRI), (c) data without radiology-pathology registration, and (d) data with increased noise (heterogeneous data from different scanners and acquisition protocols) than the internal prostate data. For clear cell RCC, using radiology image biomarkers that correlate with pathology (proposed method) as stand-alone input gave higher performance than in combination with CT images, which was not the case for the prostate. We hypothesize that for clear cell classification, the correlated features already capture the discriminating features. Adding CT increases the model complexity, degrading its performance and increases the risk of overfitting.

Our study has a few noteworthy limitations. First, the method is evaluated on clear cell RCC, and does not include other renal cancer subtypes. Secondly, by using public data, CT images taken at different post-contrast phases were included. This introduces noise in the signal to the model. A more homogeneous dataset could likely improve the models' performance, but potentially at the cost of generalizability across phases. Secondly, kidney tumors may be heterogeneous in that they have regions of both low- and high-grade areas, with more or less necrotic tissue. This granularity of tissue type was not reflected in the segmentation labels, as only a per-tumor label (indolent or aggressive) was available. However, this heterogeneity can be reflected at a global feature level by extracting high-dimensional features from entire sections (that may include normal, low-grade, high-grade and/or necrotic regions). Using radiology image biomarkers that correlate with pathology on a per-section level may therefore capture the variance in tissue types. This hypothesis is supported by the results from the prostate cohort, where this granularity of segmentation labels exists and where per-section feature aggregation gave similar or better performance compared to per-pixel. Finally, two different grading systems were used for the different cohorts, Fuhrman and ISUP. Dagher et al. (2017) showed that ISUP is a better prognostic marker than Fuhrman when using all four grades (1-4). However, when grouping the grades into low and high, only 10 cases out of 279 differed between the grad-

ing systems (all 10 cases were Fuhrman grade 3 but ISUP grade 2). The impact of using two grading systems in this study is therefore considered to be low, and where a larger variance may come from high inter-reader variability within each tumor grade system (Rabjerg et al., 2021).

Our study is the first to bring pathology information into the radiology domain for clear cell RCC characterization in the clinically relevant scenario when radiology and pathology image are not registered and pathology images are not needed during inference. Our promising results demonstrate the applicability of our approach to other diseases with unaligned radiology and pathology images. Future work will focus on increasing the cohort size, using data from multiple institutions to improve generalization, as well as the performance of our model.

5. Conclusion

In this paper, we present CorrFABR, a method of creating radiological image biomarkers by incorporating histopathology image features into the radiology domain without the need for spatially aligned data. During inference, the radiological image biomarkers can be extracted without dependence on histopathology images. We show that this approach improves performance in differentiating between indolent and aggressive clear cell renal cell carcinoma on CT compared to CT images alone. This independence of histopathology data during inference and removal of the need for spatially aligned data increases the clinical utility and relevance of the method for renal cancer characterization.

Declaration of Competing Interest

Mirabela Rusu is a paid consultant for Roche, the conflict is unrelated to this research. Also, Mirabela Rusu has research grants from Phillips Healthcare. The authors declare that they have no known competing financial interests or personal relationships that could have appeared to influence the work reported in this paper.

Acknowledgements

This work was supported by the Wallenberg AI and Autonomous Systems and Software Program (WASP-AI), the research environment ELLIIT, AIDA Vinnova grant 2017-02447, Linköping University Center for Industrial Information Technology (CENIIT), Departments of Radiology and Urology, Stanford University, GE Healthcare Blue Sky Award, National Institutes of Health, National Cancer Institute (U01CA196387 to J.D.B.), and the generous philanthropic support of our patients (G.S.). Research reported in this publication was supported by the National Cancer Institute of the National Institutes of Health under Award Number R37CA260346. The content is solely the responsibility of the authors and does not necessarily represent the official views of the National Institutes of Health.

References

- Akin, O., Elnajjar, P., Heller, M., Jarosz, R., Erickson, B.J., Kirk, S., Lee, Y., Linehan, M.W., Gautam, R., Vikram, R., Garcia, K.M., Roche, C., Bonaccio, E., Filippini, J., 2016. Radiology Data from The Cancer Genome Atlas Kidney Renal Clear Cell Carcinoma [TCGA-KIRC] collection. doi:10.7937/K9/TCIA.2016.V6PBVTDR.
- Beddy, P., Genega, E.M., Ngo, L., Hindman, N., Wei, J., Bullock, A., Bhatt, R.S., Atkins, M.B., Pedrosa, I., 2014. Tumor Necrosis on Magnetic Resonance Imaging Correlates with Aggressive Histology and Disease Progression in Clear Cell Renal Cell Carcinoma. *Clinical genitourinary cancer* 12, 55–62. doi:10.1016/j.clgc.2013.07.006.
- Bektas, C.T., Kocak, B., Yardimci, A.H., Turkcanoglu, M.H., Yucetas, U., Koca, S.B., Erdim, C., Kilickesmez, O., 2019. Clear Cell Renal Cell Carcinoma: Machine Learning-Based Quantitative Computed Tomography Texture Analysis for Prediction of Fuhrman Nuclear Grade. *European Radiology* 29, 1153–1163. doi:10.1007/s00330-018-5698-2.
- Bhattacharya, I., Lim, D.S., Aung, H.L., Liu, X., Seetharaman, A., Kunder, C.A., Shao, W., Soerensen, S.J.C., Fan, R.E., Ghanouni, P., To'o, K.J., Brooks, J.D., Sonn, G.A., Rusu, M., 2022a. Bridging the gap between prostate radiology and pathology through machine learning. *Medical Physics* 49, 5160–5181. URL: <https://onlinelibrary.wiley.com/doi/abs/10.1002/mp.15777>, doi:10.1002/mp.15777. _eprint: <https://onlinelibrary.wiley.com/doi/pdf/10.1002/mp.15777>.
- Bhattacharya, I., Seetharaman, A., Kunder, C., Shao, W., Chen, L.C., Soerensen, S.J., Wang, J.B., Teslovich, N.C., Fan, R.E., Ghanouni, P., Brooks, J.D., Sonn, G.A., Rusu, M., 2022b. Selective identification and localization of indolent and aggressive prostate cancers via CorrSigNIA: An MRI-pathology correlation and deep learning framework. *Medical Image Analysis* 75, 102288. doi:10.1016/j.media.2021.102288.
- Bhattacharya, I., Seetharaman, A., Shao, W., Sood, R., Kunder, C.A., Fan, R.E., Soerensen, S.J.C., Wang, J.B., Ghanouni, P., Teslovich, N.C., Brooks, J.D., Sonn, G.A., Rusu, M., 2020. CorrSigNet: Learning COR-Related Prostate Cancer SIGNatures from Radiology and Pathology Images for Improved Computer Aided Diagnosis, in: Martel, A.L., Abolmaesumi, P., Stoyanov, D., Mateus, D., Zuluaga, M.A., Zhou, S.K., Racoceanu, D., Joskowicz, L. (Eds.), *Medical Image Computing and Computer Assisted Intervention – MICCAI 2020*, Springer International Publishing, Cham. pp. 315–325. doi:10.1007/978-3-030-59713-9_31.
- Bhindi, B., Thompson, R.H., Lohse, C.M., Mason, R.J., Frank, I., Costello, B.A., Potretzke, A.M., Hartman, R.P., Potretzke, T.A., Boorjian, S.A., Chevillet, J.C., Leibovich, B.C., 2018. The Probability of Aggressive Versus Indolent Histology Based on Renal Tumor Size: Implications for Surveillance and Treatment. *European Urology* 74, 489–497. doi:10.1016/j.eururo.2018.06.003.
- Campbell, S., Uzzo, R.G., Allaf, M.E., Bass, E.B., Cadeddu, J.A., Chang, A., Clark, P.E., Davis, B.J., Derweesh, I.H., Giambarresi, L., Gervais, D.A., Hu, S.L., Lane, B.R., Leibovich, B.C., Pierorazio, P.M., 2017. Renal mass and localized renal cancer: Aua guideline. *The Journal of Urology* 198, 520–529. doi:10.1016/j.juro.2017.04.100.
- Capitanio, U., Bensalah, K., Bex, A., Boorjian, S.A., Bray, F., Coleman, J., Gore, J.L., Sun, M., Wood, C., Russo, P., 2019. Epidemiology of renal cell carcinoma. *European urology* 75, 74–84.
- Capitanio, U., Montorsi, F., 2016. Renal cancer. *The Lancet* 387, 894–906.
- Chandar, S., Khapra, M.M., Larochelle, H., Ravindran, B., 2016. Correlational neural networks. *Neural Computation* 28, 257–285. doi:10.1162/NECO_a__00801.
- Chen, K., Vendt, B., Smith, K., Freymann, J., Kirby, J., Koppel, P., Moore, S., Phillips, S., Maffitt, D., Pringle, M., Tarbox, L., Prior, F., 2013. The Cancer Imaging Archive (TCIA): Maintaining and Operating a Public Information Repository. *Journal of Digital Imaging* 26, 1045–1057. doi:10.1007/s10278-013-9622-7.
- Coy, H., Hsieh, K., Wu, W., Nagarajan, M.B., Young, J.R., Douek, M.L., Brown, M.S., Scalzo, F., Raman, S.S., 2019. Deep learning and radiomics: The utility of Google TensorFlow™ Inception in classifying clear cell renal cell carcinoma and oncocytoma on multiphasic CT. *Abdominal Radiology* 44, 2009–2020. doi:10.1007/s00261-019-01929-0.
- Cui, E., Li, Z., Ma, C., Li, Q., Lei, Y., Lan, Y., Yu, J., Zhou, Z., Li, R., Long, W., Lin, F., 2020. Predicting the ISUP grade of clear cell renal

- cell carcinoma with multiparametric MR and multiphase CT radiomics. *European Radiology* 30, 2912–2921. doi:10.1007/s00330-019-06601-1.
- Dagher, J., Delahunt, B., Rioux-Leclercq, N., Egevad, L., Strigley, J.R., Coughlin, G., Dunglison, N., Gianduzzo, T., Kua, B., Malone, G., Martin, B., Preston, J., Pokorny, M., Wood, S., Yaxley, J., Samaratunga, H., 2017. Clear cell renal cell carcinoma: Validation of World Health Organization/International Society of Urological Pathology grading. *Histopathology* 71, 918–925. doi:10.1111/his.13311.
- de Leon, A.D., Pedrosa, I., 2017. Imaging and Screening of Kidney Cancer. *Radiologic clinics of North America* 55, 1235–1250. doi:10.1016/j.rc1.2017.06.007.
- Demirjian, N.L., Varghese, B.A., Cen, S.Y., Hwang, D.H., Aron, M., Siddiqui, I., Fields, B.K.K., Lei, X., Yap, F.Y., Rivas, M., Reddy, S.S., Zahoor, H., Liu, D.H., Desai, M., Rhie, S.K., Gill, I.S., Duddalwar, V., 2021. CT-based radiomics stratification of tumor grade and TNM stage of clear cell renal cell carcinoma. *European Radiology* doi:10.1007/s00330-021-08344-4.
- Ding, J., Xing, Z., Jiang, Z., Chen, J., Pan, L., Qiu, J., Xing, W., 2018. CT-based radiomic model predicts high grade of clear cell renal cell carcinoma. *European Journal of Radiology* 103, 51–56. doi:10.1016/j.ejrad.2018.04.013.
- Fuhrman, S.A., Lasky, L.C., Limas, C., 1982. Prognostic significance of morphologic parameters in renal cell carcinoma. *The American Journal of Surgical Pathology* 6, 655–663. doi:10.1097/0000478-198210000-00007.
- Han, S., Hwang, S.I., Lee, H.J., 2019. The Classification of Renal Cancer in 3-Phase CT Images Using a Deep Learning Method. *Journal of Digital Imaging* 32, 638–643. doi:10.1007/s10278-019-00230-2.
- Heller, N., Isensee, F., Maier-Hein, K.H., Hou, X., Xie, C., Li, F., Nan, Y., Mu, G., Lin, Z., Han, M., Yao, G., Gao, Y., Zhang, Y., Wang, Y., Hou, F., Yang, J., Xiong, G., Tian, J., Zhong, C., Ma, J., Rickman, J., Dean, J., Stai, B., Tejpaul, R., Oestreich, M., Blake, P., Kaluzniak, H., Raza, S., Rosenberg, J., Moore, K., Walczak, E., Rengel, Z., Edgerton, Z., Vasdev, R., Peterson, M., McSweeney, S., Peterson, S., Kalapara, A., Sathianathan, N., Papanikolopoulos, N., Weight, C., 2021. The state of the art in kidney and kidney tumor segmentation in contrast-enhanced CT imaging: Results of the KiTS19 challenge. *Medical Image Analysis* 67, 101821. doi:10.1016/j.media.2020.101821.
- Hötter, A.M., Karlo, C.A., Zheng, J., Moskowitz, C.S., Russo, P., Hricak, H., Akin, O., 2016. Clear Cell Renal Cell Carcinoma: Associations Between CT Features and Patient Survival. *AJR. American journal of roentgenology* 206, 1023–1030. doi:10.2214/AJR.15.15369.
- Hsieh, J.J., Purdue, M.P., Signoretti, S., Swanton, C., Albiges, L., Schmidinger, M., Heng, D.Y., Larkin, J., Ficarra, V., 2017. Renal cell carcinoma. *Nature reviews. Disease primers* 3, 17009. doi:10.1038/nrdp.2017.9.
- Kocak, B., Durmaz, E.S., Ates, E., Kaya, O.K., Kilickesmez, O., 2019. Unenhanced CT Texture Analysis of Clear Cell Renal Cell Carcinomas: A Machine Learning–Based Study for Predicting Histopathologic Nuclear Grade. *American Journal of Roentgenology* 212, W132–W139. doi:10.2214/AJR.18.20742.
- Lin, F., Cui, E.M., Lei, Y., Luo, L.p., 2019. CT-based machine learning model to predict the Fuhrman nuclear grade of clear cell renal cell carcinoma. *Abdominal Radiology* 44, 2528–2534. URL: <https://doi.org/10.1007/s00261-019-01992-7>.
- Lin, F., Ma, C., Xu, J., Lei, Y., Li, Q., Lan, Y., Sun, M., Long, W., Cui, E., 2020. A CT-based deep learning model for predicting the nuclear grade of clear cell renal cell carcinoma. *European Journal of Radiology* 129, 109079. doi:10.1016/j.ejrad.2020.109079.
- Macenko, M., Niethammer, M., Marron, J.S., Borland, D., Woosley, J.T., Xiaojun Guan, Schmitt, C., Thomas, N.E., 2009. A method for normalizing histology slides for quantitative analysis, in: 2009 IEEE International Symposium on Biomedical Imaging: From Nano to Macro, IEEE, Boston, MA, USA. pp. 1107–1110. doi:10.1109/ISBI.2009.5193250.
- Matoso, A., Epstein, J.I., 2019. Defining clinically significant prostate cancer on the basis of pathological findings. *Histopathology* 74, 135–145. doi:10.1111/his.13712.
- Minardi, D., Lucarini, G., Mazzucchelli, R., Milanese, G., Natali, D., Gaiosi, A.B., Montironi, R., Biagini, G., Muzzonigro, G., 2005. Prognostic Role of Fuhrman Grade And Vascular Endothelial Growth Factor In pT1a Clear Cell Carcinoma In Partial Nephrectomy Specimens. *The Journal of Urology* 174, 1208–1212. doi:10.1097/01.ju.0000173078.57871.2d.
- Moch, H., Cubilla, A.L., Humphrey, P.A., Reuter, V.E., Ulbright, T.M., 2016. The 2016 WHO Classification of Tumours of the Urinary System and Male Genital Organs—Part A: Renal, Penile, and Testicular Tumours. *European Urology* 70, 93–105. doi:10.1016/j.eururo.2016.02.029.
- Morshid, A., Duran, E.S., Choi, W.J., Duran, C., 2021. A Concise Review of the Multimodality Imaging Features of Renal Cell Carcinoma. *Cureus* 13, e13231. URL: <https://www.ncbi.nlm.nih.gov/pmc/articles/PMC7946646/>, doi:10.7759/cureus.13231.
- Müller, D., Kramer, F., 2021. MIScnn: A framework for medical image segmentation with convolutional neural networks and deep learning. *BMC Medical Imaging* 21, 12. doi:10.1186/s12880-020-00543-7.
- Nazari, M., Shiri, I., Hajianfar, G., Oveisi, N., Abdollahi, H., Deevband, M.R., Oveisi, M., Zaidi, H., 2020. Noninvasive Fuhrman grading of clear cell renal cell carcinoma using computed tomography radiomic features and machine learning. *La radiologia medica* 125, 754–762. URL: <https://doi.org/10.1007/s11547-020-01169-z>, doi:10.1007/s11547-020-01169-z.
- Ning, Z., Pan, W., Chen, Y., Xiao, Q., Zhang, X., Luo, J., Wang, J., Zhang, Y., 2020. Integrative analysis of cross-modal features for the prognosis prediction of clear cell renal cell carcinoma. *Bioinformatics* 36, 2888–2895. doi:10.1093/bioinformatics/btaa056.
- Otsu, N., 1979. A threshold selection method from gray level histograms doi:10.1109/TSMC.1979.4310076.
- Padala, S.A., Barsouk, A., Thandra, K.C., Saginala, K., Mohammed, A., Vakiti, A., Rawla, P., Barsouk, A., 2020. Epidemiology of Renal Cell Carcinoma. *World Journal of Oncology* 11, 79–87. URL: <https://www.ncbi.nlm.nih.gov/pmc/articles/PMC7239575/>, doi:10.14740/wjon1279.
- Rabjerg, M., Gerke, O., Engvad, B., Marcussen, N., 2021. Comparing World Health Organization/International Society of Urological Pathology Grading and Fuhrman Grading with the Prognostic Value of Nuclear Area in Patients with Renal Cell Carcinoma. *Uro* 1, 2–13. doi:10.3390/uro1010002.
- Rasmussen, R., Sanford, T., Parwani, A.V., Pedrosa, I., 2022. Artificial intelligence in kidney cancer. *American Society of Clinical Oncology Educational Book* 42, 1–11.
- Rosales, J.C., Haramis, G., Moreno, J., Badani, K., Benson, M.C., McKiernan, J., Casazza, C., Landman, J., 2010. Active surveillance for renal cortical neoplasms. *The Journal of urology* 183, 1698–1702.
- Rusu, M., Shao, W., Kunder, C.A., Wang, J.B., Soerensen, S.J.C., Teslovich, N.C., Sood, R.R., Chen, L.C., Fan, R.E., Ghanouni, P., Brooks, J.D., Sonn, G.A., 2020. Registration of presurgical MRI and histopathology images from radical prostatectomy via RAPSODI. *Medical Physics* 47, 4177–4188. doi:10.1002/mp.14337.
- Ryu, H.S., Jin, M.S., Park, J.H., Lee, S., Cho, J., Oh, S., Kwak, T.Y., Woo, J.I., Mun, Y., Kim, S.W., Hwang, S., Shin, S.J., Chang, H., 2019. Automated Gleason Scoring and Tumor Quantification in Prostate Core Needle Biopsy Images Using Deep Neural Networks and Its Comparison with Pathologist-Based Assessment. *Cancers* 11, E1860. doi:10.3390/cancers11121860.
- Seetharaman, A., Bhattacharya, I., Chen, L.C., Kunder, C.A., Shao, W., Soerensen, S.J.C., Wang, J.B., Teslovich, N.C., Fan, R.E., Ghanouni, P., Brooks, J.D., Too, K.J., Sonn, G.A., Rusu, M., 2021. Automated detection of aggressive and indolent prostate cancer on magnetic resonance imaging. *Medical Physics* 48, 2960–2972. doi:10.1002/mp.14855.
- Shu, J., Wen, D., Xi, Y., Xia, Y., Cai, Z., Xu, W., Meng, X., Liu, B., Yin, H., 2019. Clear cell renal cell carcinoma: Machine learning-based computed tomography radiomics analysis for the prediction of WHO/ISUP grade. *European Journal of Radiology* 121, 108738. URL: <https://linkinghub.elsevier.com/retrieve/pii/S0720048X19303882>, doi:10.1016/j.ejrad.2019.108738.
- Simonyan, K., Zisserman, A., 2015. Very deep convolutional networks for large-scale image recognition, in: Bengio, Y., LeCun, Y. (Eds.), 3rd

Supplementary Material

S1. Prostate experiment, region-wise aggregation

In Table S1, results are included in the intermediate step where slice and in-plane correspondence between the radiology and pathology data exists, but where features are aggregated on a per-region basis (both lesion-TMA/biopsy and lesion-section). Results showing where this correspondence has been removed is also presented as comparison, as well as in Table 3.

- International Conference on Learning Representations, ICLR 2015, San Diego, CA, USA, May 7-9, 2015, Conference Track Proceedings. URL: <http://arxiv.org/abs/1409.1556>.
- Sun, X., Liu, L., Xu, K., Li, W., Huo, Z., Liu, H., Shen, T., Pan, F., Jiang, Y., Zhang, M., 2019. Prediction of isup grading of clear cell renal cell carcinoma using support vector machine model based on ct images. *Medicine* 98.
- Sun, X.Y., Feng, Q.X., Xu, X., Zhang, J., Zhu, F.P., Yang, Y.H., Zhang, Y.D., 2020. Radiologic-Radiomic Machine Learning Models for Differentiation of Benign and Malignant Solid Renal Masses: Comparison With Expert-Level Radiologists. *American Journal of Roentgenology* 214, W44–W54. doi:10.2214/AJR.19.21617.
- Sung, H., Ferlay, J., Siegel, R.L., Laversanne, M., Soerjomataram, I., Jemal, A., Bray, F., 2021. Global Cancer Statistics 2020: GLOBOCAN Estimates of Incidence and Mortality Worldwide for 36 Cancers in 185 Countries. *CA: A Cancer Journal for Clinicians* 71, 209–249. doi:10.3322/caac.21660.
- Tanaka, T., Huang, Y., Marukawa, Y., Tsuboi, Y., Masaoka, Y., Kojima, K., Iguchi, T., Hiraki, T., Gobara, H., Yanai, H., Nasu, Y., Kanazawa, S., 2020. Differentiation of Small (≤ 4 cm) Renal Masses on Multiphase Contrast-Enhanced CT by Deep Learning. *American Journal of Roentgenology* 214, 605–612. doi:10.2214/AJR.19.22074.
- Tse, J.R., Shen, L., Shen, J., Yoon, L., Kamaya, A., 2021. Prevalence of Malignancy and Histopathological Association of Bosniak Classification, Version 2019 Class III and IV Cystic Renal Masses. *The Journal of Urology* 205, 1031–1038. doi:10.1097/JU.0000000000001438.
- Uhm, K.H., Jung, S.W., Choi, M.H., Shin, H.K., Yoo, J.I., Oh, S.W., Kim, J.Y., Kim, H.G., Lee, Y.J., Youn, S.Y., Hong, S.H., Ko, S.J., 2021. Deep learning for end-to-end kidney cancer diagnosis on multiphase abdominal computed tomography. *npj Precision Oncology* 5, 54. doi:10.1038/s41698-021-00195-y.
- Xie, S., Tu, Z., 2017. Holistically-Nested Edge Detection. *International Journal of Computer Vision* 125, 3–18. doi:10.1007/s11263-017-1004-z.
- Xv, Y., Lv, F., Guo, H., Zhou, X., Tan, H., Xiao, M., Zheng, Y., 2021. Machine learning-based CT radiomics approach for predicting WHO/ISUP nuclear grade of clear cell renal cell carcinoma: An exploratory and comparative study. *Insights into Imaging* 12, 170. doi:10.1186/s13244-021-01107-1.
- Yan, L., Liu, Z., Wang, G., Huang, Y., Liu, Y., Yu, Y., Liang, C., 2015. Angiomyolipoma with Minimal Fat. *Academic Radiology* 22, 1115–1121. doi:10.1016/j.acra.2015.04.004.
- Zhang, L., Zha, Z., Qu, W., Zhao, H., Yuan, J., Feng, Y., Wu, B., 2018. Tumor necrosis as a prognostic variable for the clinical outcome in patients with renal cell carcinoma: a systematic review and meta-analysis. *BMC Cancer* 18, 870. URL: <https://doi.org/10.1186/s12885-018-4773-z>, doi:10.1186/s12885-018-4773-z.
- Zigeuner, R., Hutterer, G., Chromecki, T., Imamovic, A., Kampel-Kettner, K., Rehak, P., Langner, C., Pummer, K., 2010. External Validation of the Mayo Clinic Stage, Size, Grade, and Necrosis (SSIGN) Score for Clear-Cell Renal Cell Carcinoma in a Single European Centre Applying Routine Pathology. *European Urology* 57, 102–111. doi:10.1016/j.eururo.2008.11.033.
- Zuo, T., Zheng, Y., He, L., Chen, T., Zheng, B., Zheng, S., You, J., Li, X., Liu, R., Bai, J., Si, S., Wang, Y., Zhang, S., Wang, L., Chen, J., 2021. Automated Classification of Papillary Renal Cell Carcinoma and Chromophobe Renal Cell Carcinoma Based on a Small Computed Tomography Imaging Dataset Using Deep Learning. *Frontiers in Oncology* 11. doi:10.3389/fonc.2021.746750.

Correlated Feature Aggregation by Region

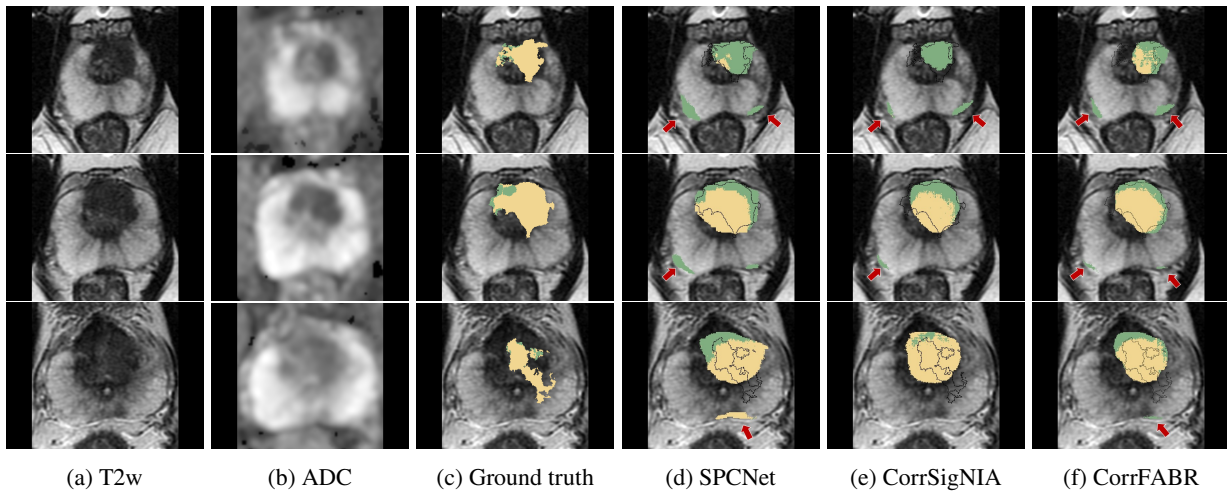


Figure S1: Example of a patient from the prostate test cohort, showing three slices. The three left-most panels show T2w, ADC and T2w with ground truth segmentations overlaid. The right-most panels show prediction results for (d) SPCNet, (e) CorrSigNIA (pixel-pixel CorrFeat), and (f) CorrFABR (lesion-section CorrFeat), with ground truth overlaid (black outline). Arrows shows examples of false positive predictions.

Table S1

Lesion-wise results for clinically significant prostate cancer, showing results with and without slice correspondence (E1).

Method	Resolution	Slice Corr.	Feat. Aggregation	Input	ROC-AUC	Dice	Sensitivity	Specificity
SPCNet	N/A	N/A	None	MRI	0.86 ± 0.28	0.36 ± 0.19	0.86 ± 0.34	0.48 ± 0.35
CorrSigNIA	Low	✓	Pixel-pixel	MRI + CorrFeat	0.87 ± 0.29	0.37 ± 0.21	0.86 ± 0.34	0.60 ± 0.37
CorrFABR	Low	✓	Lesion-TMA/biopsy	MRI + CorrFeat	0.87 ± 0.26	0.35 ± 0.23	0.82 ± 0.38	0.64 ± 0.39
CorrFABR	Low	-	Lesion-TMA/biopsy	MRI + CorrFeat	0.89 ± 0.27	0.36 ± 0.21	0.82 ± 0.37	0.53 ± 0.36
CorrFABR	Low	✓	Lesion-section	MRI + CorrFeat	0.90 ± 0.25	0.38 ± 0.21	0.90 ± 0.29	0.64 ± 0.36
CorrFABR	Low	-	Lesion-section	MRI + CorrFeat	0.90 ± 0.22	0.36 ± 0.19	0.94 ± 0.22	0.51 ± 0.37
CorrFABR	Low	✓	Lesion-section	CorrFeat	0.87 ± 0.31	0.38 ± 0.23	0.86 ± 0.34	0.76 ± 0.31
CorrFABR	High	-	Lesion-section	MRI + CorrFeat	0.87 ± 0.31	0.36 ± 0.22	0.86 ± 0.34	0.59 ± 0.37
CorrFABR	High	-	Lesion-section	CorrFeat	0.84 ± 0.30	0.32 ± 0.21	0.82 ± 0.38	0.49 ± 0.34

Table S2

Tumor diameter in cm. For KiTS21, radiologic measurements are given. For TCGA-KIRC, approximations of diameter based on calculated volume from automatic segmentations are given. TCGA-KIRC has no Grade 1 cases.

Tumor Grade	Grade 1	Grade 2	Grade 3	Grade 4
KiTS21	3.24 ± 1.17	4.07 ± 2.31	6.27 ± 3.67	8.49 ± 2.70
TCGA-KIRC	-	4.96 ± 2.60	5.82 ± 2.72	8.00 ± 3.01

Table S3

Number of cases with/without necrosis per tumor grade. Bold numbers indicate cases defined as aggressive (with necrosis and/or tumor grade 3 or 4).

	Without Necrosis	With Necrosis	Total
Grade 1	24	0	24
Grade 2	149	19	168
Grade 3	107	27	134
Grade 4	23	23	46
Total	303	69	372